Materials Horizons

ROYAL SOCIETY OF CHEMISTRY

COMMUNICATION

View Article Online
View Journal | View Issue

Cite this: *Mater. Horiz.*, 2026, **13**, 1313

Received 29th August 2025,
Accepted 31st October 2025

DOI: 10.1039/d5mh01657f

rsc.li/materials-horizons

A bioinspired polyoxo-titanium cluster for efficient photocatalytic CO_2 reduction assisted by hydrogen bonding

Shiming Zhang,[ab] Guoxiang Zhao,[a] Yayu Yan,[ab] Qiao-Hong Li,[a] Hai-Xia Zhang,[a] Xin Wu*[a] and Jian Zhang*[a]

Designing functional sites with well-defined and directional photocatalytic activities is crucial for efficiently utilizing spatially separated photogenerated charge carriers and achieving high photocatalytic performance. Herein, inspired by natural photosynthesis, we successfully developed a series of phosphonic acid functionalized polyoxo-titanium clusters. We uncover the pivotal role of strategically positioning noncovalent interactions surrounding the catalytic center in regulating the CO_2 reduction performance. Remarkably, introducing amino groups in synergy with proton-rich phosphate moieties near the cobalt-nitrogen active site leads to a six-fold enhancement in photocatalytic CO_2 reduction activity. Among them, the modified cluster NH_2-BQTiCo delivers an exceptional CO_2 photoreduction performance under visible light, achieving a CO production rate as high as 1456 μmol g^{-1} h^{-1}. Combining experimental results with DFT calculations reveals that strong intermolecular hydrogen-bonding traction around the catalytical center can significantly strengthen CO_2 adsorption and facilitate a smoother activation pathway. This work highlights a biomimetic design strategy to optimize electron delocalization within polyoxo-titanium clusters, thereby promoting efficient intramolecular charge transfer and advancing high-performance CO_2 photoreduction.

New concepts

This work introduces a biomimetic strategy of engineering directional noncovalent interactions in the secondary coordination sphere of cobalt–nitrogen active sites within polyoxo-titanium clusters (PTCs) to dramatically enhance photocatalytic CO_2 reduction. Unlike previous studies focusing primarily on active center modification, we emphasize the critical role of precisely positioned proton-donors (phosphonate) and electron-donors (amino groups) in forming strong hydrogen-bonding networks that synergistically strengthen CO_2 adsorption and lower activation barriers. This approach diverges from conventional catalyst design by leveraging microenvironment control to facilitate efficient intramolecular charge delocalization and smooth proton-coupled electron transfer. It provides a fundamental insight into how supramolecular interactions mimic enzymatic catalysis to optimize photocatalytic performance, offering a generalized paradigm for designing next-generation molecular photocatalysts with atomic precision.

1. Introduction

The direct conversion of solar energy into chemical energy through photocatalytic technology represents one of the most promising strategies for developing a sustainable alternative to fossil fuels and addressing the global energy crisis.[1–4] Among various approaches, photocatalytic CO_2 reduction, which harnesses sunlight to transform carbon dioxide into value-added chemicals such as methanol, ethanol, and methane, offers a dual advantage: mitigating atmospheric CO_2 levels while providing renewable pathways for energy conversion and storage.[5–7] However, the intrinsic thermodynamic stability of CO_2 and the high dissociation energy of the C═O bond impose substantial kinetic and energetic barriers to its activation.[8] Consequently, current photocatalytic efficiencies remain insufficient to meet industrial demands and still fall far short of the capabilities achieved by natural photosynthesis. To overcome these challenges, researchers have increasingly drawn inspiration from biological systems. In natural enzymes, the strategic arrangement of noncovalent interactions around catalytic centers can significantly enhance selectivity, activity, and stability. This principle has been successfully translated into the design of molecular, supramolecular and heterogeneous systems. Nevertheless, achieving precise control over the periphery of the active sites remains synthetically challenging in non-biological systems.

Polyoxo-titanium clusters (PTCs) represent a unique class of molecularly defined, nanoscale compounds comprising titanium-oxo cores surrounded by tunable organic ligands. Functioning as molecular analogs of bulk titanium dioxide (TiO_2), PTCs provide atomic-level insights into the structure–property relationships

[a] *State Key Laboratory of Structural Chemistry, Fujian Institute of Research on the Structure of Matter, Chinese Academy of Sciences, Fuzhou, Fujian 350002, P. R. China. E-mail: wuxin@fjirsm.ac.cn, zhj@fjirsm.ac.cn*
[b] *University of Chinese Academy of Sciences, Beijing 100049, P. R. China*

while combining the synthetic versatility of organometallic complexes with the robustness of semiconductor materials. Their well-defined architectures allow for precise manipulation of active-site composition, spatial organization, and surrounding surface functionalities, thereby enabling rational tailoring of their electronic structures and reactivities. Consequently, PTCs have been extensively explored for diverse photocatalytic applications, including CO_2 reduction, hydrogen production, degradation of organic pollutants, and hydrogen peroxide generation.[9–12] However, pristine Ti-oxo systems generally suffer from wide band gaps (>3.0 eV), limiting their light absorption to the ultraviolet region.[13] Moreover, sluggish charge transport and insufficient CO_2 binding sites further hinder their overall photocatalytic performance.

Herein, we report a rationally designed polyoxo-titanium cluster photocatalyst functionalized with pendant amino groups and proton-rich phosphate moieties. The introduction of electron-donating NH_2 groups, in synergy with phosphate ligands acting as proton carriers, enables the formation of directional charge-assisted hydrogen bonds that stabilize local microenvironments around the cobalt–nitrogen active sites. These engineered non-covalent interactions within the secondary coordination sphere strengthen CO_2 adsorption and facilitate its activation, thereby significantly boosting the photocatalytic CO_2 reduction activity.[14] This work provides new insights into the biomimetic design of titanium-oxo cluster-based photocatalysts and offers a general strategy for enhancing photocatalytic performance through fine-tuned control of active-site microenvironments.

2. Results and discussion

We successfully synthesized four structurally related titanium-oxo clusters, namely $[Ti_4(\mu_3\text{-}O)(\mu_2\text{-}O^iPr)_3(O^iPr)_5(O_3P\text{-}Phen)_3]_2(PZ)$ (BQTi), $[Ti_4(\mu_3\text{-}O)(\mu_2\text{-}O^iPr)_3(O^iPr)_3(O_3P\text{-}Phen)_3]_2(APZ)$ (NH_2-BQTi), $[Ti_3Co(\mu_3\text{-}O)(\mu_2\text{-}O^iPr)_3(O^iPr)_3(O_3P\text{-}Phen)_3]_2(PZ)$ (BQTiCo) and $[Ti_3Co(\mu_3\text{-}O)(\mu_2\text{-}O^iPr)_3(O^iPr)_3(O_3P\text{-}Phen)_3]_2(APZ)$ (NH_2-BQTiCo), where O_3P-Phen = phenyl phosphonate, bim = benzimidazole, O^iPr = isopropoxide, PZ = pyrazine and APZ = 2-aminopyrazine. As illustrated in Fig. 1a, NH_2-BQTiCo was synthesized *via* a solvothermal reaction in isopropanol using titanium(IV) isopropoxide, $Co(NO_3)_2{\cdot}6H_2O$, 2-aminopyrazine, and phenylphosphonic acid, yielding high-purity blue block-shaped crystals. BQTi, NH_2-BQTi, and BQTiCo were obtained under similar conditions, as detailed in the SI. Single-crystal X-ray diffraction (SCXRD) analysis revealed that all four crystals crystallize in the monoclinic system with the $P\bar{1}$ space group. The crystallographic parameters and structure refinement details are summarized in Table S1 and S2. The NH_2-BQTiCo cluster consists of six hexacoordinated Ti ions and two tetracoordinated Co ions. Each Ti ion adopts an octahedral geometry, coordinated by six oxygen atoms from two phenylphosphonate ligands, one μ_3-O ion, and three isopropyl groups. Three Ti ions and six isopropyl groups are connected *via* μ_3-O ions, forming a Ti_3 subunit. This subunit was further connected to Co ions *via* three phenylphosphonic acid ligands, while the two Co ions were linked to nitrogen atoms on 2-aminopyrazine, forming the overall cluster structure. The molecular structures of BQTi, NH_2-BQTi BQTiCo and NH_2-BQTiCo resemble an "automobile wheel" (Fig. S1), where the Ti_4 or $[Ti_3Co]$ core acts as a "three-spoked wheel", while the coordinated ligands behave as "bearings" (Fig. 1b).[15] The clusters self-assemble into extended three-dimensional structures (Fig. S2–S5). Notably, the presence of pendant amino groups ($-NH_2$) and proton-rich phosphate moieties induces directional charge-assisted hydrogen bonding within the secondary coordination sphere (Fig. S6), where the N–H···O hydrogen bonds (2.72–2.85 Å) stabilize the local environment around the Co–N active sites. Bond valence sum (BVS) calculations indicated that all Ti ions adopt a +4 oxidation state, while the Co ion exists in the +2 state (Table S3–S6), consistent with the SCXRD results.

The phase purity and crystallinity of the materials were examined using powder X-ray diffraction (PXRD). As shown in

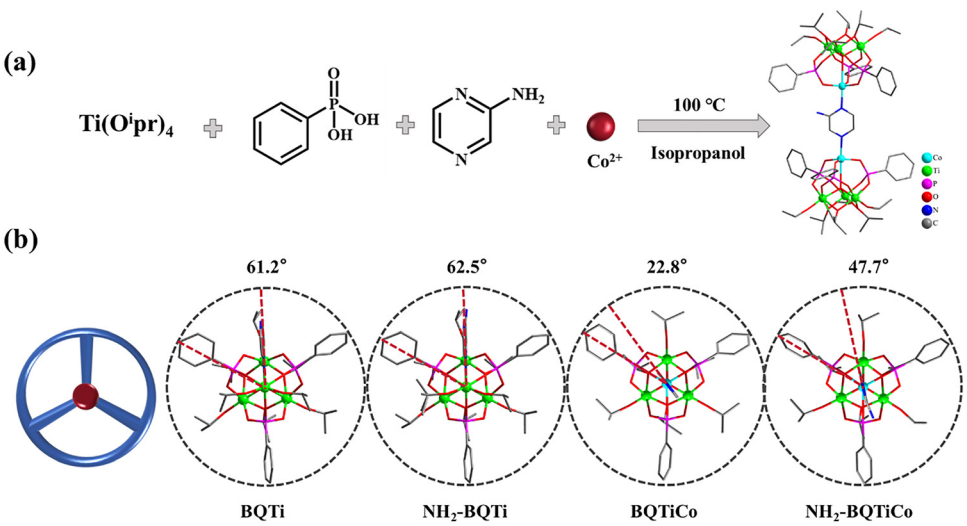

Fig. 1 (a) Schematic representation of the synthesis process and (b) the schematic diagram of BQTi, NH_2-BQTi, BQTiCo and NH_2-BQTiCo. Ti = green, Co = turquoise, P = purple, N = blue, O = red, and C = gray.

Fig. S7 and S8, the experimental diffraction patterns match well with the simulated profiles, confirming the formation of phase-pure, highly crystalline compounds. Fourier-transform infrared (FT-IR) spectroscopy was employed to identify the functional groups (Fig. S9). Characteristic peaks at 1000–1300 cm^{-1} and 750–1000 cm^{-1} correspond to in-plane and out-of-plane C–H bending vibrations, respectively. The peaks observed at 1610–1370 cm^{-1} are assigned to the skeletal vibrations of the pyrazine ring, while those at 1670–1340 cm^{-1} correspond to the stretching vibrations of C=C and C–N bonds.[16] Additionally, a broad absorption band at 3300–3500 cm^{-1} is attributed to the stretching vibration of the NH_2 groups, confirming the successful incorporation of amino functionalities.

The elemental composition and surface electronic states of the sample were characterized using X-ray photoelectron spectroscopy (XPS). The survey spectrum confirmed the presence of C, O, N, P, Ti, and Co elements, demonstrating the successful incorporation of Co into the Ti clusters (Fig. S10a). In the high-resolution Ti 2p spectrum (Fig. S10b), peaks at 458.97 eV and 464.72 eV correspond to the Ti $2p_{3/2}$ and Ti $2p_{1/2}$ orbitals, respectively, consistent with the Ti^{4+} oxidation state in the Ti clusters.[17] The Co 2p spectrum shows characteristic Co^{2+} peaks at 780.94 eV ($2p_{3/2}$) and 796.70 eV ($2p_{1/2}$), accompanied by two satellite peaks, confirming the divalent state of Co (Fig. S10c).[18] Notably, following the introduction of NH_2 groups, the binding energies of the Co elements in NH_2-BQTiCo experience a negative shift relative to BQTi, while the Ti element undergoes a positive shift. The observed shifts suggest the formation of a stable Lewis acid–base coordination between N and Co, facilitating electron transfer and increasing the electron density around the Co sites. Complementary energy-dispersive X-ray spectroscopy (EDS) further confirmed the presence of C, O, N, P, Ti, and Co elements in the material (Fig. S11–S14).

To elucidate the catalytic effect of the as-synthesized photocatalyst, we explored its photocatalytic activity for CO_2 reduction. The photocatalytic CO_2 reduction performance of the prepared materials is summarized in Fig. 2a. For all samples, the primary reduction products were CO and H_2. Among them, NH_2-BQTiCo exhibited the highest catalytic activity, achieving remarkable CO and H_2 production rates of 1456 μmol g^{-1} h^{-1} and 862 μmol g^{-1} h^{-1}, respectively (Fig. 2b). Furthermore, NH_2-BQTiCo also demonstrated the highest CO_2 adsorption capacity of 4.68 cm^3 g^{-1} (Fig. S15b). The superior CO_2 conversion efficiency of NH_2-BQTiCo can be attributed to the formation of directional hydrogen bonds between the amino groups and phosphate oxygens, which can facilitate CO_2 adsorption and activation. Additionally, the local polarization effects induced by N–Co coordination further promote efficient charge separation, ultimately enhancing the CO_2 photoreduction performance. To comprehensively evaluate the photocatalytic CO_2 reduction activity of NH_2-BQTiCo, its efficiency was tested under various light wavelengths. The maximum apparent quantum yield for CO_2 reduction was determined to be 0.523% at 450 nm (Fig. S16). This value is higher than other reported titanium-containing metal–organic frameworks and cluster materials in Table S7. To investigate the influence of different reaction conditions, a series of control experiments were conducted (Fig. 2c). No detection of CO_2 reduction products was observed

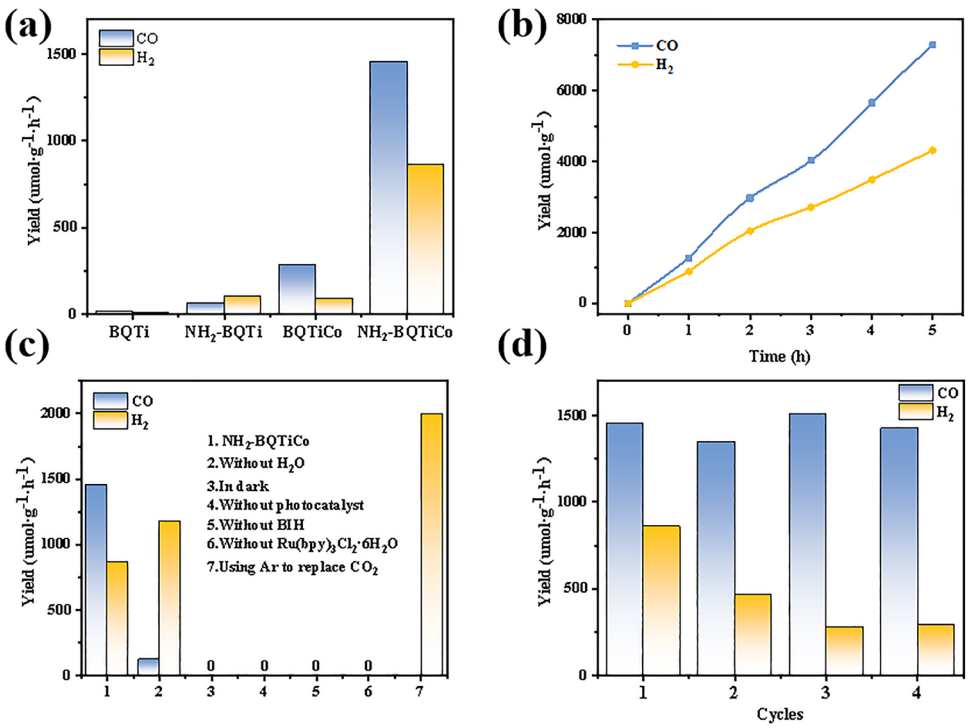

Fig. 2 (a) CO and H_2 yields of BQTi, NH_2-BQTi, BQTiCo and NH_2-BQTiCo; (b) CO and H_2 production trend of NH_2-BQTiCo; (c) CO_2 reduction performance under different condition experiments and (d) CO_2 reduction cycling experiment.

in the absence of either light or photocatalyst, confirming that photogenerated charge carriers are indispensable and that light absorption is essential to drive the reaction. Moreover, no CO was observed when the reaction was carried out under an Ar atmosphere, verifying that CO_2 gas is the sole carbon source in the system. Interestingly, when no external H_2O was supplied, CO production decreased significantly. This is because H_2O oxidation generates protons (H^+) and O_2, and the presence of H^+ is crucial for facilitating CO_2 conversion, highlighting the essential role of water in the photocatalytic process. Recycling tests showed (Fig. 2d) that the catalytic performance of NH_2-BQTiCo remained stable after four consecutive cycles, demonstrating excellent reusability. The XRD analysis (Fig. S17) after the reaction also showed that the material maintains good crystallinity, indicating its excellent stability. Additionally, thermogravimetric analysis (TGA, Fig. S18) confirmed the material's thermal robustness. The intramolecular hydrogen bonding between amino and phosphate groups suppresses molecular motion, thereby enhancing structural stability, while N–Co coordination bonds further strengthen the lattice framework.[19] Collectively, these results demonstrate that NH_2-BQTiCo possesses outstanding thermal and chemical stability, and excellent reusability, making it a promising candidate for efficient photocatalytic CO_2 reduction.

The optical absorption properties of the synthesized photocatalysts were examined using UV-vis diffuse reflectance spectroscopy (UV-vis DRS, Fig. 3a). Upon cobalt incorporation, the light absorption of NH_2-BQTiCo in the visible region is enhanced by promoting efficient electronic coupling. Meanwhile, the introduction of amino groups acts synergistically by donating electrons to the π-conjugated framework, thereby promoting π-electron delocalization and establishing additional charge-transfer pathways. As a result, NH_2-functionalized Co-containing clusters exhibit superior visible-light harvesting capabilities compared to their pristine counterparts.

The optical band gaps, estimated from Tauc plots (Fig. S19), are approximately 2.90 eV for BQTi, 2.85 eV for NH_2-BQTi, 1.75 eV for BQTiCo, and 1.70 eV for NH_2-BQTiCo, respectively. These results indicate that the simultaneous introduction of NH_2 groups and Co centers efficiently narrows the bandgap through either an upward shift of the valence band maximum (VBM) or a downward shift of the conduction band minimum (CBM). This bandgap narrowing not only expands visible-light absorption into longer-wavelengths but also improves the generation and separation of photogenerated carriers.

The electronic structures of the materials were further analyzed using Mott–Schottky (M–S) plots (Fig. S20). All four clusters exhibit positive slopes, confirming their n-type semiconducting behavior. The estimated flat-band potentials are approximately −0.72 V for BQTi, −0.75 V for NH_2-BQTi, −0.92 V for BQTiCo, and −0.93 V for NH_2-BQTiCo. For n-type semiconductors, the conduction band (CB) minimum typically lies ~0.197 V more negative than the flat-band potential.[20] Accordingly, the CB positions of BQTi, NH_2-BQTi, BQTiCo, and NH_2-BQTiCo are determined to be −0.52 V, −0.55 V, −0.72 V, and −0.73 V *versus* the normal hydrogen electrode (*vs.* NHE), respectively. The energy position of the CB edge of the

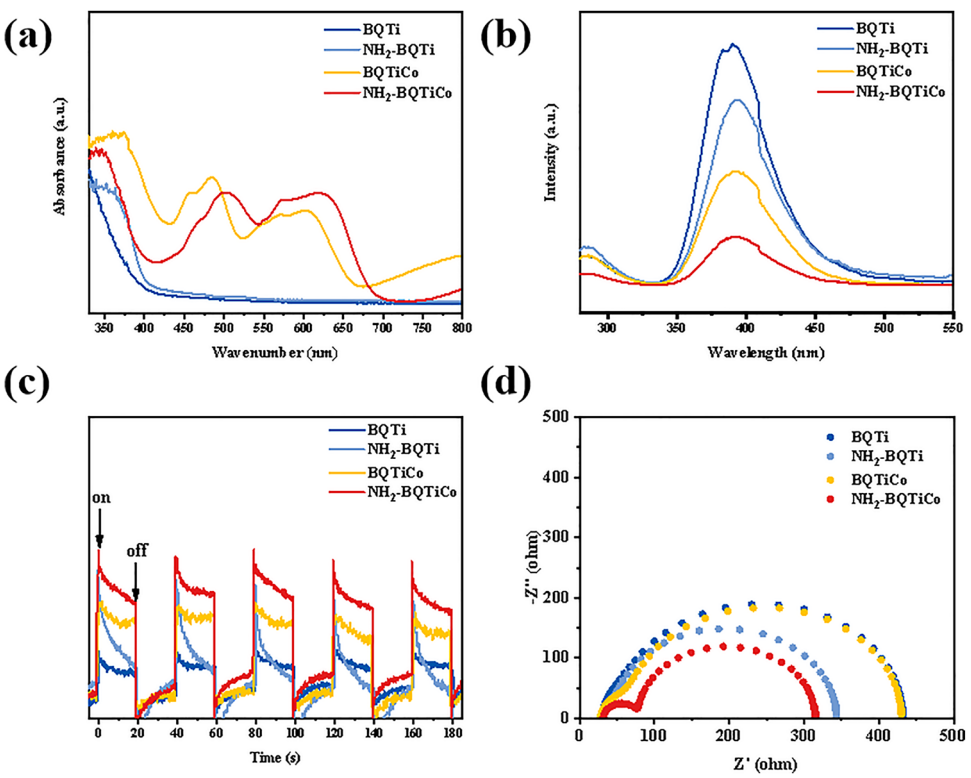

Fig. 3 (a) The UV-vis DRS of BQTi, NH_2-BQTi, BQTiCo and NH_2-BQTiCo; (b) photoluminescence spectra; (c) electrochemical impedance spectroscopy; (d) transient photocurrent response spectra.

NH_2-BQTiCo is more negative than those of BQTi, NH_2-BQTi, and BQTiCo, and it is theoretically feasible that photogenerated electrons transfer from the CB to the active sites in NH_2-BQTiCo. Based on the above results, the corresponding band structure alignment of the four materials is illustrated in Fig. S21.

The charge separation and transfer dynamics were further investigated *via* photoluminescence (PL) spectra, transient photocurrent response (*I*–*t*) curves, and electrochemical impedance spectroscopy (EIS) measurements (Fig. 3b–d). Among the tested samples, NH_2-BQTiCo exhibits the lowest PL intensity, implying minimal radiative recombination and highly efficient separation of photogenerated electron–hole pairs. Correspondingly, NH_2-BQTiCo demonstrates the highest photocurrent response and the smallest Nyquist radius in the EIS profile, further indicating its enhanced light utilization efficiency, more effective charge separation, and faster interfacial charge transfer kinetics. The reduced Nyquist radius corresponds to a lower charge transfer resistance (R_{ct}), reflecting enhanced electron transfer at the catalyst-electrolyte interface. Such characteristics are thermodynamically favorable, as they reduce the activation energy required for the charge transfer process. These improvements can be attributed to the dual role of the Co centers. They can act as electron traps, capturing photogenerated electrons and thereby suppressing their recombination. Moreover, the coordination between the lone pair electrons of the nitrogen and Co induces local polarization, establishing a directional internal electric field that promotes rapid carrier separation and facilitates efficient charge transfer.

To gain a deeper insight into the surface reaction intermediates involved in CO_2 reduction, *in situ* diffuse reflectance infrared Fourier transform spectroscopy (DRIFTS) was performed on the BQTi and NH_2-BQTiCo photocatalysts (Fig. 4a–c). Compared with BQTi, NH_2-BQTiCo exhibited significantly stronger CO_2 adsorption, as evidenced by the enhanced IR absorption bands. Distinct characteristic peaks were observed at 1325 cm^{-1} and 1365 cm^{-1} (monodentate carbonate, m-CO_3^{2-}), 1445 cm^{-1} (bicarbonate, HCO_3*), and 1536 cm^{-1} (bidentate carbonate, b-CO_3^{2-}),[21–23] indicating that both CO_2 and H_2O were effectively adsorbed and activated on the surface of NH_2-BQTiCo. Under visible-light irradiation, an additional absorption peak emerged at 1635 cm^{-1}, which was attributed to the symmetric stretching vibration of the adsorbed COOH* intermediate,[24] a key species in the CO_2 reduction pathway. Based on these findings, a mechanistic pathway for photocatalytic CO_2 reduction over NH_2-BQTiCo is proposed in Fig. 4d. Upon visible-light excitation, NH_2-BQTiCo generates photoinduced electrons and holes. In the presence of $[Ru(bpy)_3]Cl_2 \cdot 6H_2O$ as a photosensitizer, the photogenerated electrons are efficiently transferred to the catalyst surface to reduce CO_2 into CO, while the holes are consumed by sacrificial agents or water oxidation. The equation presented below illustrates all the successive reaction steps:

$$NH_2\text{-BQTiCo} + h\nu \rightarrow e^- + h^+ \quad (1)$$

$$H_2O + 2h^+ \rightarrow 2H^+ + 1/2O_2 \quad (2)$$

$$CO_2 + e^- + H^+ \rightarrow COOH^* \quad (3)$$

$$COOH^* + e^- + H^+ \rightarrow CO^* + H_2O \quad (4)$$

$$CO^* \rightarrow CO\uparrow \quad (5)$$

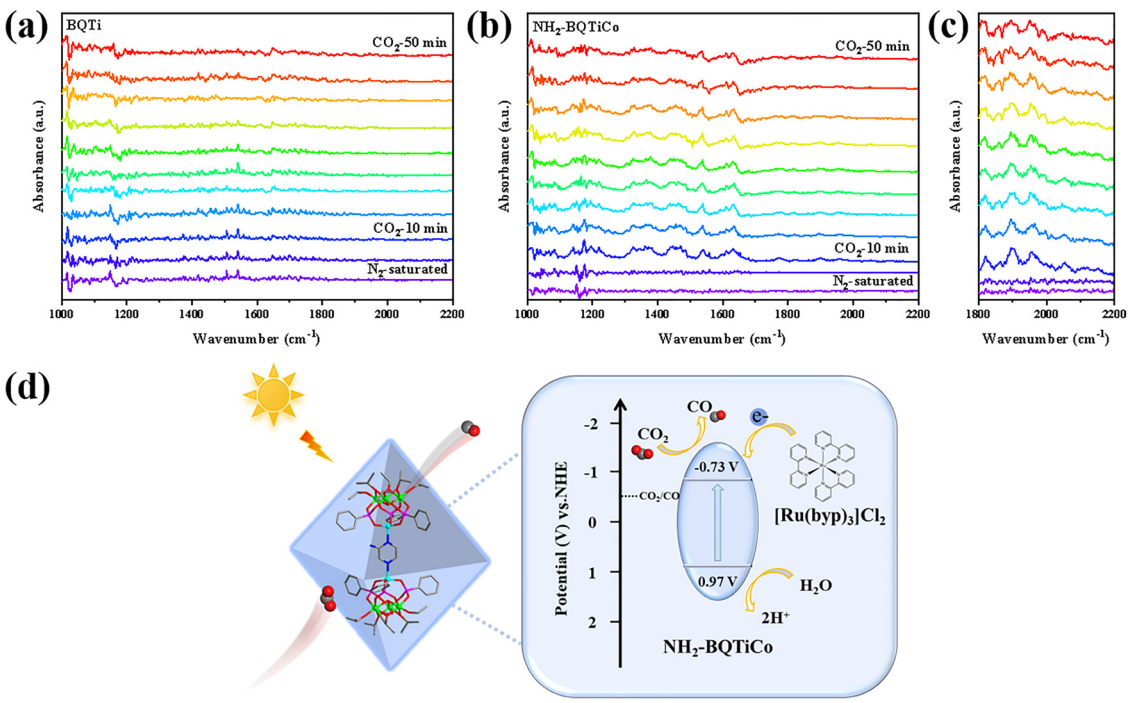

Fig. 4 (a) *In situ* FTIR spectra of CO_2 adsorption on the BQTi surface: (b) and (c) *in situ* FTIR spectra of CO_2 adsorption on the NH_2-BQTiCo surface; (d) the possible CO_2 photoreduction mechanism of the NH_2-BQTiCo.

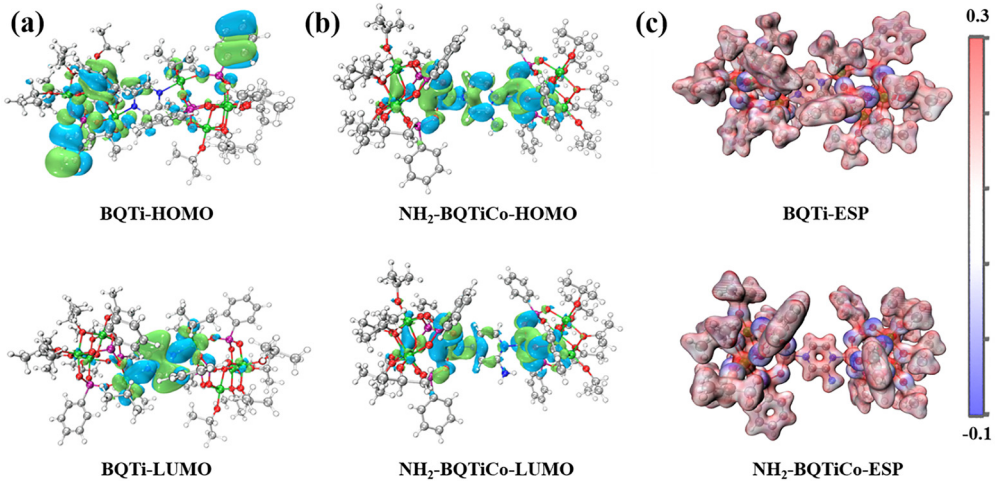

Fig. 5 The HOMO and LUMO of BQTi (a) and NH_2-BQTiCo (b); The electrostatic potential of BQTi and NH_2-BQTiCo (c).

Further DFT calculations were undertaken, aimed at elucidating the photocatalytic reaction mechanism of the polyoxygenated titanium clusters. Based on first-principles calculations, we analyzed the frontier molecular orbitals of the two compounds (Fig. 5a and b). The results indicate that the highest occupied molecular orbital (HOMO) of BQTi was primarily localized on the O atoms and the benzenephosphonic acid ligand, while the lowest unoccupied molecular orbital (LUMO) was mainly distributed over the Ti center and the pyrazine ligand, suggesting the possibility of ligand-to-metal charge transfer (LMCT). In contrast, both the HOMO and LUMO of NH_2-BQTiCo were highly localized on the Co and 2-aminopyrazine unit, indicating a metal–ligand localized electronic transition. This spatial confinement may help restrict the photogenerated electron–hole pairs near the active site, potentially suppressing their recombination and thereby enhancing photocatalytic efficiency.

Furthermore, molecular electrostatic potential (ESP) analysis reveals that in both BQTi and NH_2-BQTiCo, the O atoms serve as the main regions of negative potential (nucleophilic sites), whereas the metal centers (Ti/Co) exhibited positive potential (electrophilic sites) (Fig. 5c). This polarized charge distribution suggests that during photocatalytic processes, the O atoms are likely to act as electron donors, while the metal centers may function as electron acceptors, thereby facilitating interfacial charge separation and subsequent redox reactions.

3. Conclusions

In summary, we successfully synthesized a series of polyoxotitanium cluster photocatalysts in which metal ions are coordinated with different pyrazine ligands. The introduction of nitrogen–cobalt coordination bonds induces localized electronic polarization, which facilitates charge separation and transfer. Meanwhile, the incorporation of pendant base groups and proton-rich phosphate units constructs functional outer coordination spheres, enabling directional binding interactions and promoting efficient proton-coupled electron transfer. Benefiting from these synergistic enhancements, NH_2-BQTiCo exhibits outstanding photocatalytic CO_2 reduction activity, achieving an optimal CO production rate of 1456 μmol g^{-1} h^{-1}. This work demonstrates a new design strategy for improving the photocatalytic performance of titanium-oxo cluster-based catalysts by modulating their electronic structure and engineering tailored surface interactions, offering valuable insights for the rational design of advanced photocatalysts for efficient solar-to-fuel conversion. Future work will focus on enhancing photocatalytic efficiency by incorporating multiple active sites and developing more robust, multifunctional materials for efficient CO_2 reduction under challenging conditions.

Author contributions

Shiming Zhang – conceptualization, methodology, formal analysis, and writing original draft; Guoxiang Zhao – theoretical calculations, writing review and editing; Yayu Yan – theoretical calculations, writing review and editing; Qiaohong Li – resources and investigation; Hai-Xia Zhang – resources and investigation; Xin Wu – writing review and editing and supervision; Jian Zhang – resources, writing review and editing, supervision, and project administration.

Conflicts of interest

The authors declare no conflict of interest.

Data availability

All supporting data (including crystallographic data, structure refinement parameters, and experimental methods) have been deposited in the supplementary information (SI). See DOI: https://doi.org/10.1039/d5mh01657f.

CCDC 2468206–2468208 contain the supplementary crystallographic data for this paper.[25a–c]

Acknowledgements

This work is supported by the National Key Research and Development Program of China (2021YFA1501500), the National Natural Science Foundation of China (22275192), and Fujian Provincial Natural Science Foundation (2024J01188).

References

1 Y. Han, Y. Yan, Q. Li, X. Wu, F. Wang and J. Zhang, *Sci. China Chem.*, 2025, **68**, 3028–3033.
2 W. Wang, S. Wang, X. Ma and J. Gong, *Chem. Soc. Rev.*, 2011, **40**, 3703–3727.
3 H. Takeda, K. Ohashi, A. Sekine and O. Ishitani, *J. Am. Chem. Soc.*, 2016, **138**, 4354–4357.
4 Z. Guo, S. Cheng, C. Cometto, E. Anxolabehere-Mallart, S. M. Ng, C. C. Ko, G. Liu, L. Chen, M. Robert and T. C. Lau, *J. Am. Chem. Soc.*, 2016, **138**, 9413–9416.
5 H. Peng, X. Deng, G. Li, Q. Wang, M. Song, P. Chen and S.-F. Yin, *Appl. Catal., B*, 2022, **318**, 121866.
6 Y. Xi, W. Mo, Z. Fan, L. Hu, W. Chen, Y. Zhang, P. Wang, S. Zhong, Y. Zhao and S. Bai, *J. Mater. Chem. A*, 2022, **10**, 20934–20945.
7 R. Kuriki, H. Matsunaga, T. Nakashima, K. Wada, A. Yamakata, O. Ishitani and K. Maeda, *J. Am. Chem. Soc.*, 2016, **138**, 5159–5170.
8 Z. Miao, Q. Wang, Y. Zhang, L. Meng and X. Wang, *Appl. Catal., B*, 2022, **301**, 12080.
9 Z. Jiang, J. Liu, M. Gao, X. Fan, L. Zhang and J. Zhang, *Adv. Mater.*, 2017, **29**, 1603369.
10 X. Wu, Q. H. Li, S. Zuo, Y. Li, X. Yi, L. B. Yuan, L. Zheng, J. Zhang, J. Dong, S. Wang, H. Zhang and J. Zhang, *Nano Lett.*, 2023, **23**, 11562–11568.
11 W. H. Fang, L. Zhang and J. Zhang, *J. Am. Chem. Soc.*, 2016, **138**, 7480–7483.
12 K. Su, M. Wu, Y. Tan, W. Wang, D. Yuan and M. Hong, *Chem. Commun.*, 2017, **53**, 9598–9601.
13 J. X. Liu, M. Y. Gao, W. H. Fang, L. Zhang and J. Zhang, *Angew. Chem., Int. Ed.*, 2016, **55**, 5160–5165.
14 N. Li, S. J. Yao, M. J. Wei, J. He, W. Chi and Y. Q. Lan, *Small*, 2023, **19**, e2206724.
15 H. Fu, X. Wu, W.-H. Fang, L. Zhang, F. Wang and J. Zhang, *Inorg. Chem. Front.*, 2021, **8**, 4102–4106.
16 H. Wang, Y. Ding, M. Ning, M. Yu, W. Zheng, X. Ruan, Y. Xi, Y. Dai, H. Liu and G. He, *Sep. Purif. Technol.*, 2023, **322**, 124227.
17 M. Gao, S. Zhang, Y. Yan, Z. Qian, L. Qin, X. Liu, Q. R. Ding, Q. Li, X. Wu and J. Zhang, *Dalton Trans.*, 2025, **54**, 9016–9020.
18 W. Lu, C. E. Tait, G. Avci, X. Li, A. E. Crumpton, P. Shao, C. M. Aitchison, F. Ceugniet, Y. Yao, M. D. Frogley, D. Decarolis, N. Yao, K. E. Jelfs and I. McCulloch, *J. Am. Chem. Soc.*, 2025, **147**, 9056–9061.
19 C. Yao, S. Zhang, S. Zuo, W. Liu, Y. Kong, X. Liu, X. Wang and C. Ni, *Mater. Lett.*, 2014, **126**, 135–138.
20 J. Sun, Y. Hou, Z. Yu, L. Tu, Y. Yan, S. Qin, S. Chen, D. Lan, H. Zhu and S. Wang, *J. Hazard. Mater.*, 2021, **419**, 126543.
21 X. Li, L. Li, G. Chen, X. Chu, X. Liu, C. Naisa, D. Pohl, M. Löffler and X. Feng, *Nat. Commun.*, 2023, **14**, 4034.
22 S. Yu, L. Tan, S. Bai, C. Ning, G. Liu, H. Wang, B. Liu, Y. Zhao and Y. F. Song, *Small*, 2022, **18**, 2202334.
23 S. Zhang, Y. Rong, J. Wei, Z. Li, T. Liang, Z. Yu, H. Zhu, S. Wang and Y. Hou, *J. Colloid Interface Sci.*, 2023, **629**, 604–615.
24 S. Zhang, S. Fan, T. Liang, J. Wei, T. Zhu, Y. Shen, Z. Yu, H. Zhu, S. Wang and Y. Hou, *J. Colloid Interface Sci.*, 2023, **652**, 1126–1137.
25 (*a*) CCDC 2468206: Experimental Crystal Structure Determination, 2025, DOI: **10.5517/ccdc.csd.cc2nvckg**; (*b*) CCDC 2468207: Experimental Crystal Structure Determination, 2025, DOI: **10.5517/ccdc.csd.cc2nvclh**; (*c*) CCDC 2468208: Experimental Crystal Structure Determination, 2025, DOI: **10.5517/ccdc.csd.cc2nvcmj**.